MESH STUDY FOR A DIRECT NUMERICAL SIMULATION OF THE TRANSONIC FLOW AT Re_c=500,000 AROUND A NACA 0012 AIRFOIL

Manuel A. Gageik, Igor Klioutchnikov and Herbert Olivier,
Shock Wave Laboratory, RWTH Aachen University

Abstract

Performing a Direct Numerical Simulation (DNS), a mesh study for the transonic flow around the well known NACA 0012 airfoil at a moderate Reynolds number of $Re_c = 5 \cdot 10^5$ is presented. The three-dimensional Navier-Stokes equations for an unsteady, compressible flow are discretized in a generalized curvilinear coordinate system. The spatial derivatives of first-order are approximated by a fifth-order WENO scheme, the second-order derivatives by a sixth-order central scheme and the time derivatives by a fourth-order Runge-Kutta scheme. The focus of the investigation is on the demonstration of the applicability of DNS for simulating an airfoil flow at a moderate Reynolds number. At this Reynolds number, theoretical estimations for the necessary number of mesh points are far away from realizable mesh sizes. In the present study five three-dimensional meshes are compared where the largest mesh consists of one billion mesh points (8192 x 512 x 256). This mesh size is close to the practical limit of recent simulations since the numerical effort, expressed in core-hours, is $16 \cdot 10^6 \ h$. The other meshes are gradually coarsened by a factor of 0.25 resulting in only four million mesh points for the coarsest mesh. The mesh study is performed by the comparison of aerodynamical and turbulent quantities. On the one hand the main flow features are studied, which are mostly determined by large flow scales. On the other hand the turbulent intensities are compared, which are influenced by the smallest scales. In this context, the analysis of the energy-spectrum of the turbulent kinetic energy is a useful tool to evaluate the quality of the turbulent boundary layer. Furthermore, pressure waves are studied for all meshes which are generated at the trailing-edge moving upstream.

1 INTRODUCTION

Direct Numerical Simulations (DNS) of the transonic flow around the well known NACA 0012 airfoil at a moderate Reynolds number of $Re_c = 5 \cdot 10^5$ based on the chord length c are performed for five meshes. The focus of the investigation is the study of the applicability of DNS for simulating a wall bounded airfoil flow at a moderate Reynolds number. Wall bounded flow means that the turbulent structures appear only near the wall of the airfoil and its wake and not in all regions of the mesh, resulting in the possibility to coarsen the mesh.

In contrast to other numerical methods that use standard turbulence or subgrid-scale models, in a DNS, the smallest scales of turbulences have to be resolved since the original Navier-Stokes equations are numerically solved without any turbulence modelling. In DNS, flow structures which are smaller than the mesh spacing are not resolved. In this context, a DNS of a turbulent flow around an airfoil at real flight conditions ($Re_c > 10^7$) is with today's available resources not possible. The necessary number of mesh points causes a computational effort that exceeds the recent capabilities of super computers. For the present case a general estimation of the necessary mesh points can be done by the formula $N_{3D} = Re_c^{(9/4)}$ and results in $N_{3D} = 6.6 \cdot 10^{12}$ for $Re_c = 5 \cdot 10^5$. In a recent publication, Choi [1] estimates the number of mesh points, necessary for a DNS of a wall bounded turbulent flow, to $N_{DNS,Moin} \sim Re_{L_x}^{37/14}$ with the streamwise length of the flat plate L_x. Both approximations consider uniform mesh resolutions in streamwise, spanwise and wall-normal direction. Although the performance of supercomputers grows exponentially and it has reached the petascale computing, it is reasonable to assume that such a fully resolved DNS of an airfoil flow at even this relatively low Reynolds number is not possible for the next years. Nevertheless, both estimations are not fair and very conservative due to the fact that the flow is wall bounded. Therefore, by clustering mesh points in viscous zones (boundary layer, wake) and stretching the mesh in the inviscid flow area, the number of required mesh points can be reduced significantly. The practically required number of mesh points is much lower but cannot be defined a priori. Consequently, a mesh convergence study for DNS has a big scientific and practical worth since it is very rare in literature because of its enormous computational cost.

Tucker and DeBonis [2] summarizes the recent situation of so called near-direct solutions (NDS) which involves large eddy simulations and quasi-direct numerical simulations. Depending on the flow which is simulated (airframe, aeroengine, aeroacoustic), an eddy resolving simulation will be possible within the next decades. Lele and Nichols [3] predict that non-wall bounded flows at high Reynolds numbers can be simulated by NDS within the next 5-10 years. In this context, the present

study allows to quantify the error of under resolved but recently practicable DNS compared to a reasonably highly resolved DNS.

It has to be noted that the flow is wall bounded and a high-order numerical method is applied. The positive influence of the wall bounded flow on the number of mesh points has already been mentioned. Another important factor is the spatial and temporal order of the used numerical method. Moin and Mahesh [4] points out the lower resolution requirements for high-order schemes. Comparing a second- and a fourth-order central difference scheme, it is easy to show that the required mesh resolution of the second-order scheme is approximately twice the one of the fourth-order reaching the same accuracy.

2 DIRECT NUMERICAL SIMULATION

The numerical method and its governing equations have also been used in former publications which show a good agreement with experimental results [5].

2.1 Governing equations

The three-dimensional Navier-Stokes equations for an unsteady, compressible flow in curvilinear coordinates are used in conservative non-dimensional form:

$$\frac{\partial U}{\partial t} + \frac{\partial F}{\partial \xi} + \frac{\partial G}{\partial \eta} + \frac{\partial H}{\partial \zeta} = \frac{\partial F^\nu}{\partial \xi} + \frac{\partial G^\nu}{\partial \eta} + \frac{\partial H^\nu}{\partial \zeta} \quad (1)$$

Here, the solution vector U, the inviscid fluxes F, G, H and the viscous fluxes F^ν, G^ν, H^ν are defined as

$$U = J \begin{pmatrix} \rho \\ \rho u \\ \rho v \\ \rho w \\ \rho e \end{pmatrix}, \quad F = J \begin{pmatrix} \rho \theta_1 \\ \rho \theta_1 u + \xi_x p \Upsilon \\ \rho \theta_1 v + \xi_y p \Upsilon \\ \rho \theta_1 w + \xi_z p \Upsilon \\ \rho \theta_1 \left(e + \frac{p}{\rho} \Upsilon \right) \end{pmatrix}$$

$$G = J \begin{pmatrix} \rho \theta_2 \\ \rho \theta_2 u + \eta_x p \Upsilon \\ \rho \theta_2 v + \eta_y p \Upsilon \\ \rho \theta_2 w + \eta_z p \Upsilon \\ \rho \theta_2 \left(e + \frac{p}{\rho} \Upsilon \right) \end{pmatrix}, \quad H = J \begin{pmatrix} \rho \theta_3 \\ \rho \theta_3 u + \zeta_x p \Upsilon \\ \rho \theta_3 v + \zeta_y p \Upsilon \\ \rho \theta_3 w + \zeta_z p \Upsilon \\ \rho \theta_3 \left(e + \frac{p}{\rho} \Upsilon \right) \end{pmatrix}$$

$$F^\nu = J \begin{pmatrix} 0 \\ \Psi \left(\xi_x \tau_{\xi\xi} + \xi_y \tau_{\xi\eta} + \xi_z \tau_{\xi\zeta} \right) \\ \Psi \left(\xi_x \tau_{\xi\eta} + \xi_y \tau_{\eta\eta} + \xi_z \tau_{\eta\zeta} \right) \\ \Psi \left(\xi_x \tau_{\xi\zeta} + \xi_y \tau_{\eta\zeta} + \xi_z \tau_{\zeta\zeta} \right) \\ \Psi(u \left(\xi_x \tau_{\xi\xi} + \xi_y \tau_{\xi\eta} + \xi_z \tau_{\xi\zeta} \right) + \\ v \left(\xi_x \tau_{\xi\eta} + \xi_y \tau_{\eta\eta} + \xi_z \tau_{\eta\zeta} \right) + \\ w \left(\xi_x \tau_{\xi\zeta} + \xi_y \tau_{\eta\zeta} + \xi_z \tau_{\zeta\zeta} \right)) + \\ \Gamma \left(\xi_x q_\xi + \xi_y q_\eta + \xi_z q_\zeta \right) \end{pmatrix} \quad (2)$$

$$G^\nu = J \begin{pmatrix} 0 \\ \Psi \left(\eta_x \tau_{\xi\xi} + \eta_y \tau_{\xi\eta} + \eta_z \tau_{\xi\zeta} \right) \\ \Psi \left(\eta_x \tau_{\xi\eta} + \eta_y \tau_{\eta\eta} + \eta_z \tau_{\eta\zeta} \right) \\ \Psi \left(\eta_x \tau_{\xi\zeta} + \eta_y \tau_{\eta\zeta} + \eta_z \tau_{\zeta\zeta} \right) \\ \Psi(u \left(\eta_x \tau_{\xi\xi} + \eta_y \tau_{\xi\eta} + \eta_z \tau_{\xi\zeta} \right) + \\ v \left(\eta_x \tau_{\xi\eta} + \eta_y \tau_{\eta\eta} + \eta_z \tau_{\eta\zeta} \right) + \\ w \left(\eta_x \tau_{\xi\zeta} + \eta_y \tau_{\eta\zeta} + \eta_z \tau_{\zeta\zeta} \right)) + \\ \Gamma \left(\eta_x q_\xi + \eta_y q_\eta + \eta_z q_\zeta \right) \end{pmatrix}$$

$$H^\nu = J \begin{pmatrix} 0 \\ \Psi \left(\zeta_x \tau_{\xi\xi} + \zeta_y \tau_{\xi\eta} + \zeta_z \tau_{\xi\zeta} \right) \\ \Psi \left(\zeta_x \tau_{\xi\eta} + \zeta_y \tau_{\eta\eta} + \zeta_z \tau_{\eta\zeta} \right) \\ \Psi \left(\zeta_x \tau_{\xi\zeta} + \zeta_y \tau_{\eta\zeta} + \zeta_z \tau_{\zeta\zeta} \right) \\ \Psi(u \left(\zeta_x \tau_{\xi\xi} + \zeta_y \tau_{\xi\eta} + \zeta_z \tau_{\xi\zeta} \right) + \\ v \left(\zeta_x \tau_{\xi\eta} + \zeta_y \tau_{\eta\eta} + \zeta_z \tau_{\eta\zeta} \right) + \\ w \left(\zeta_x \tau_{\xi\zeta} + \zeta_y \tau_{\eta\zeta} + \zeta_z \tau_{\zeta\zeta} \right)) + \\ \Gamma \left(\zeta_x q_\xi + \zeta_y q_\eta + \zeta_z q_\zeta \right) \end{pmatrix}$$

$$\Theta_1 = u\xi_x + v\xi_y + w\xi_z, \ \Theta_2 = u\eta_x + v\eta_y + w\eta_z,$$
$$\Theta_3 = u\zeta_x + v\zeta_y + w\zeta_z$$
$$\Upsilon = \frac{1}{\gamma Ma_\infty^2}, \ \Psi = \frac{1}{Re_\infty}, \ \Gamma = \frac{1}{(\gamma - 1) Ma_\infty^2 Pr_\infty}$$

where $\xi_{x,y,z}$, $\eta_{x,y,z}$, $\zeta_{x,y,z}$ are the metric coefficients and J is the Jacobian of the transformation of the Cartesian coordinates x, y and z into the curvilinear coordinates $\xi(x,y,z)$, $\eta(x,y,z)$ and $\zeta(x,y,z)$. The perfect gas law relates the density ρ, the pressure p and the temperature T whereas the viscosity μ is calculated by Sutherland's law. τ and q are the transformed shear stress tensor and heat flux vector, respectively. The total energy e is defined as

$$e = \frac{u^2 + v^2 + w^2}{2} + \frac{\Upsilon}{\gamma - 1} \frac{p}{\rho}, \quad (3)$$

The ratio of the specific heats γ is set to 1.4 and the Prandtl number Pr_∞ is 0.72. For the nondimensionalization of the equations (1)-(3) following reference variables are used: $L_{ref} = c \ (chord \ length) = 0.08 \ m$, $T_\infty = 300 \ K$, u_∞, p_∞ and μ_∞.

2.2 Numerical method

For time integration an explicit, fourth-order, low storage Runge-Kutta scheme is applied. The viscous fluxes F^ν, G^ν and H^ν are approximated by using a sixth-order central-difference scheme. The inviscid fluxes F, G and H are approximated by using a fifth-order

Weighted Essentially Non-Oscillatory (WENO) finite difference scheme corresponding to Jiang and Shu [6]. Exemplary for the flux in ξ-direction, the scheme is explained in the following. The derivative of the flux F at the mesh point i is given as

$$\left(\frac{\partial F}{\partial \xi}\right)_i = \frac{F_{i+1/2} - F_{i-1/2}}{\Delta \xi} \tag{4}$$

where the cell boundary fluxes $F_{i+\frac{1}{2}}$ are

$$F_{i+\frac{1}{2}} = \sum_{m=0}^{r-1} \omega_m M_m^r \tag{5}$$

$$M_m^r = \sum_{l=i+m-r+1}^{i+m} a_{m,l}^r F_l.$$

M_m^r is the $m-th$ of r ($r = (N+1)/2 = 3$) sub-stencils with polynomial coefficients $a_{m,l}^r$ for a fifth-order of approximation ($N = 5$). The normalized weighting coefficient ω_m, defined as

$$\omega_m = \frac{\bar{\omega}_m}{\bar{\omega}_0 + ... + \bar{\omega}_{r-1}} \qquad \bar{\omega}_m = \frac{b_m^r}{(\epsilon + IS_m)^2}, \tag{6}$$

preserves monotonicity in the vicinity of strong gradients by the means of the smoothness indicators IS_m. The parameter ϵ is added to avoid a division by zero at smooth solutions and is set to $\epsilon \approx 10^{-150}$ which is close to the minimal floating point value. The coefficients b_m^r are called optimal coefficients for the fifth-order of accuracy in smooth solution regions.

In order to improve the numerical stability of the scheme, the propagation direction of the characteristics is taken into account resulting in a decomposition of the fluxes into two parts

$$F_{i+1/2} = F_{i+1/2}^+ + F_{i+1/2}^- \tag{7}$$

where the algebraic sign of the eigenvalue λ of the matrix $A = \partial F/\partial U$ determines the propagation direction. Matrix A can be transformed into the characteristic form $A = R\Lambda R^{-1}$ with the diagonal matrix of eigenvalues Λ, the right eigenvector R and the left eigenvector R^{-1}. Due to the usage of the maximal eigenvalue $\lambda_{i,max}$ within the stencil, it is called a local Lax-Friedrichs flux-vector splitting. Finally, it yields to

$$F_{i+1/2} = \overbrace{\frac{1}{12}\left[-F_{i-1} + 7F_i + 7F_{i+1} - F_{i+2}\right]}^{central\ term} +$$

$$\sum_{s=1}^{5}\left[-\Phi_N\left(R_s^{-1}\Delta F_{i-3/2}^{s,+}, ... R_s^{-1}\Delta F_{i+3/2}^{s,+}\right)\right. \tag{8}$$

$$\left.+\Phi_N\left(R_s^{-1}\Delta F_{i+5/2}^{s,-}, ... R_s^{-1}\Delta F_{i-1/2}^{s,-}\right)\right]R_s$$

$$\Delta F_{i+1/2}^{s,\pm} = F_{i+1}^{s,\pm} - F_i^{s,\pm}$$

$$F_i^{s,\pm} = \frac{1}{2}\left(F_i^s \pm \lambda_{i,max}\hat{U}_i^s\right)$$

where the function Φ_N computes the non-linear corrections added to the central term depending on the weighting coefficients shown in equation (6), the $s-th$ component of the flux differences $\Delta F_{i+1/2}^{s,\pm}$ and the eigenvectors R_s and R_s^{-1}.

2.3 Configuration

For the mesh study a NACA 0012 airfoil is considered at the transonic flow conditions $M_\infty = 0.65$, $Re_c = 5 \cdot 10^5$ and an angle of incidence of $\alpha = 2°$. The mesh size in spanwise direction is $L_z = 0.1c$. The distance between the airfoil and the upper boundary of the computed regime is approximately $L_y \approx 30c$ (slightly different for all meshes). The distance between the trailing-edge (TE) and the outflow boundary is $L_x = 8c$. In spanwise direction the mesh is equidistant. At the leading-edge (LE) and the TE, the streamwise mesh points are clustered. In wall-normal direction, the mesh is extruded starting with an initial wall-normal mesh spacing which is the smallest spacing of the mesh. Fulfilling the requirement $\Delta y_{wall} < 1 \cdot y^+$, in a preliminary two-dimensional study, the first wall-normal mesh spacing is determined to $\Delta y_{wall} = 40c/Re_c = 8 \cdot 10^{-5}c$ for all meshes. In the results, see Tab. 2, it is shown that this estimation is too optimistic and the computed y^+ becomes larger than unity in the area of maximal turbulent wall friction. Since the Courant-Friedrichs-Lewy condition ($CFL = \lambda\Delta t/\Delta x$) links the mesh spacing Δx and time step Δt, this smallest mesh spacing is of great influence on the computational effort. On this account this value is a compromise between essential mesh requirements for DNS and the possibility to achieve quasi-stationary results in practice.

Depending on the wall-normal mesh points, the meshes' growth factors and consequently the number of points within the boundary layer are different. In the fourth column of Tab. 1, the number of the mesh points are listed, at which the height of the boundary layer δ_{99} at the TE is reached.

In summary, the results for five meshes have been studied, shown in Tab. 1. The finest mesh has about one billion mesh points and its size is close to the practical limit of recent simulations since the numerical effort, expressed in core-hours, is $16 \cdot 10^6\ h$. The other meshes are gradually coarsened in streamwise direction by a factor of 0.5 and alternately in wall-normal and spanwise direction additionally by a factor of 0.5.

Mesh	resolution	size [mio.]	$j_{\delta_{99},TE}$
Mesh 1 (M1)	512x128x64	4	64
Mesh 2 (M2)	1024x128x128	17	66
Mesh 3 (M3)	2048x256x128	67	79
Mesh 4 (M4)	4096x256x256	268	79
Mesh 5 (M5)	8192x512x256	1.074	227

Tab. 1: Attributes of studied meshes

3 Results

First, the temporal convergence to a quasi-stationary solution is studied for all meshes. It has to be noted that the number of time steps is a critical parameter, especially for DNS. On the one hand, the solution has to converge to a quasi-stationary state, and on the other hand, the computational costs have to be taken into account. The process of convergence behaves asymptotically with simulated time steps and is dependent on the flow parameters. Therefore, it is difficult to formulate an exact point of convergence. In the present study, the analysis of integral values (coefficients for lift c_L and drag c_D) showed a very fast convergence. The reason for this is that integral values neglect some kind of oscillations. For example, if the pressure rises simultaneously on the upper and lower side of the airfoil, this rise skipts out in the formula for lift and the resulting integral value remains constant. As a result, the local pressure coefficient at the LE is considered for the convergence study (see Fig. 1). This location has the advantage that it is not superposed by instantaneous disturbances, which occur in the turbulent flow at the TE, for example.

At *time step* $= 0$, the two-dimensional solution is used to initialize the computation on the mesh M5. After $322,500$ *time steps*, the simulations with the meshes M1-M4 are initialized starting from M5. It has to be noted that the results for the mesh M5 were already present when the mesh study was performed. This explains the unconventional procedure (interpolating results from a fine mesh onto a coarser mesh instead vice versa). As a consequence of the initialization, the results of M1-M4, shown in Fig. 1, illustrate large disturbances shortly after initialization. The symbols and colors of the graphs, which are used for the different meshes, are the same for all figures in this paper. The coarser the grid, the lower is the number of mesh points compared to M5 and the stronger is the initial disturbance of the solution. Within the simulated time, this disturbance vanishes for all meshes. Recalling the use of c_L and c_D for a convergence study, both parameters show significantly weaker the initialization disturbances since the disturbances occur on the upper and lower airfoil surface simultaneously. It is reasonable to assume that an asymptotic convergence is achieved for all meshes and that further time steps would show only slight changes in the solution. Since the time scales

of turbulence are much lower than the one of pressure waves, which are studied in Fig. 1, the turbulent quantities are in a quasi-stationary state, too.
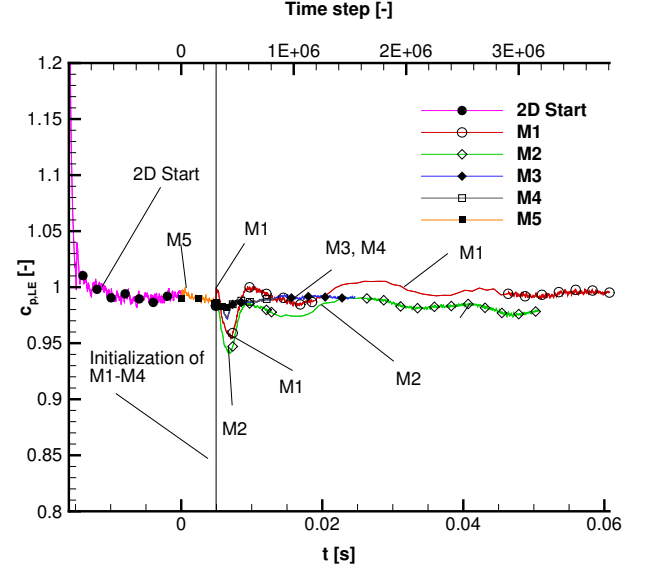

Fig. 1: Convergence behaviour for all meshes

In Fig. 2 the pressure and friction coefficients are illustrated. Considering the c_f graphs of the suction side, for M3, M4 and M5, transition occurs at $x/c \approx 0.45$ and for M1 and M2 further downstream. On the pressure side, transition starts at $x/c \approx 0.88$ depending on the mesh size. The transition begins at distinguishable different positions where the finer meshes show the transition more upstream than the coarser ones. This is obvious by both, the pressure and the suction side transition behaviour. Beside the areas of transition, for the pressure coefficient, the agreement of all graphs is very good, especially for the meshes M3, M4 and M5.

The skin-friction coefficient reacts much more sensitive to the mesh size since it is computed by the velocity gradient, $c_f = 2\tau_{wall}/(\rho u) = 2\mu(\partial u/\partial y)_{wall}/(\rho u)$. At the stagnation point, c_f is maximal and decreases while moving downstream. This decrease, within the laminar boundary layer, agrees well for all meshes. Indicating a widespread area of boundary layer separation, the skin-friction coefficients become negative at $x/c = 0.26$. In the vicinity of the transition, c_f drops further and then rises due to the transition to a turbulent boundary layer. Its rise significantly depends on the number of mesh points in spanwise direction. Coarser meshes underestimate significantly c_f. The differences of two meshes having the same number of spanwise mesh points (M2-M3 and M4-M5) are negligible denoting the importance of the spanwise resolution.

Sensitive parameters (location of transition, skin-friction coefficient) show differences between the meshes. The main flow features (pressure distribution, appearance of transition on both airfoil sides, boundary layer separation regions) are detectable for all meshes.
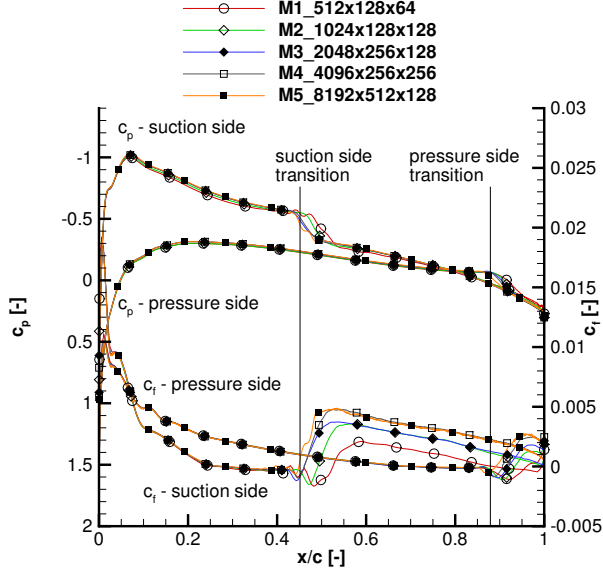

Fig. 2: Pressure and friction coefficients along airfoil

Tabel 2 lists the spanwise as well as time averaged wall units, taken at the mesh dependent location of the maximum turbulent $c_{f,max}$ on the suction side. Additionally, Δy_{TE}^+ is presented. It is interesting to note, that the coarse meshes show a lower Δy^+. This is a result of the underestimated velocity gradient which is also visible in the lower c_f-values for the coarser meshes (see Fig. 2). The lower the velocity gradient, the larger the viscous length scale δ_ν becomes. For coarser meshes, this leads to a lower $\Delta y^+ = \Delta y_{wall}/\delta_\nu$ since Δy_{wall} is constant for all meshes. In the area of $c_{f,max}$ the wall-normal spacing Δy^+ is larger than unity. At the TE, Δy_{TE}^+ is smaller than unity. With hindsight, the first wall-normal spacing is slightly too large.
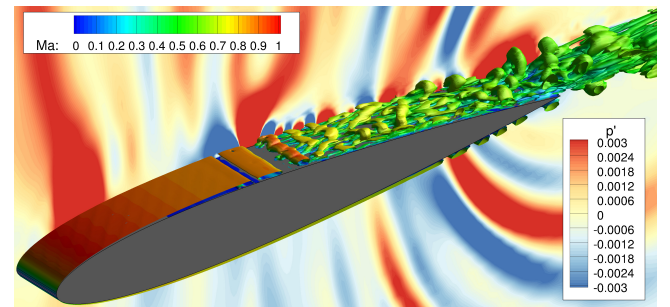
Mesh	Δx^+	Δy^+	Δz^+	Δy_{TE}^+
M1	72.7	1.1	21.7	0.2
M2	47.8	1.4	14.1	0.3
M3	24.0	1.4	14.1	0.3
M4	14.0	1.7	8.3	0.7
M5	8.7	1.7	8.2	0.7

Tab. 2: Wall units of studied meshes

Figures 3a-e visualize the flow around the NACA 0012 airfoil at $M_\infty = 0.65$, $Re_c = 5 \cdot 10^5$ and an incidence of $\alpha = 2°$. Colored by the local Mach number, iso-surfaces of the positive second invariant of the velocity gradient, Q-criterion, illustrate structures of the

boundary layer flow. In the laminar part of the boundary layer, the iso-surfaces are smooth. For the shown iso-surfaces, here, the flow velocity is maximal and the Mach number reaches about one. Then, in the region of transition, the large scale Tollmien-Schlichting (TS) waves become visible which finally break down to smaller scales. On the suction side, the boundary layer becomes turbulent at approximately the half of the chord length and on the pressure side, this happens close to the TE. The shape factor drops to $H = 1.4$ for M2-M5 at $x/c = 0.55$ indicating that the transition ends and the turbulent boundary layer starts. The mesh M1 does not reach $H = 1.4$ but $H = 1.7$. On the pressure side, the shape factors for all meshes reaches the turbulent range just at the TE. Therefore, it can be assumed that the boundary layer is still influenced by transitional processes like the TS-waves. Hence, in the following, the pressure side boundary layer is called transitional boundary layer. As a result of the interaction of the turbulent and the transitional boundary layer at the TE, the tonal noise phenomenon occurs for this flow condition. In contrast to the interaction of two turbulent boundary layers generating broadband noise, the emitted pressure waves are dominated by one tonal frequency. In this case, the frequency of the upstream moving pressure waves is equivalent to the frequency of the TS-waves. The colours of the slice in the background are determined by instantaneous pressure fluctuations ($p' = p(t) - 1/T \int p(t)dt$). For all meshes, the tonal pressure waves generated at the TE are detectable. This confirms the assumption that on the pressure side the TS-waves reach the TE.

On the suction side in the vicinity of the LE, the flow becomes supersonic influencing the propagation of pressure waves. Since supersonic regions prevent acoustic waves from a further upstream movement, acoustic waves steepen resulting in shock waves that are able to pass the supersonic region. For the meshes M3-M5, the shock waves are distinguishable in the vicinity of the LE as single sharp red lines.
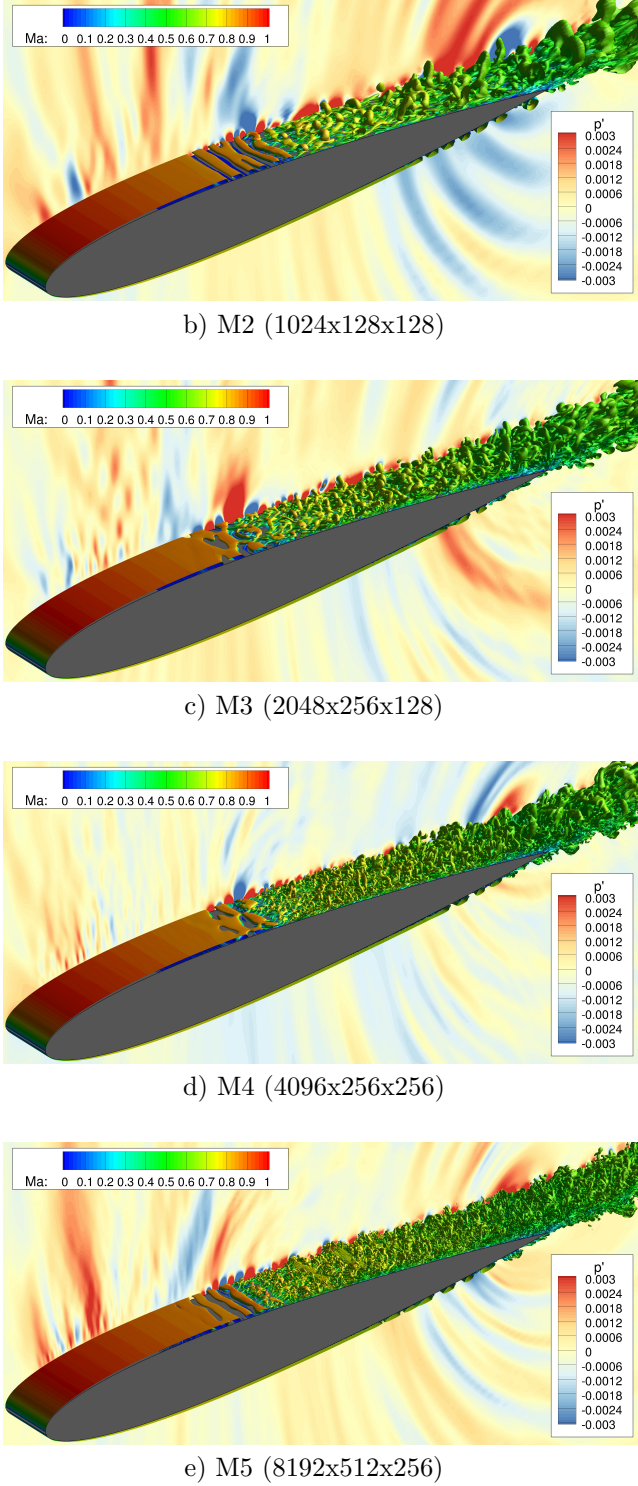

a) M1 (512x128x64)

b) M2 (1024x128x128)

c) M3 (2048x256x128)

d) M4 (4096x256x256)

e) M5 (8192x512x256)

Fig. 3: Q-criterion isosurfaces (Q=1) coloured by Mach numbers, slice coloured by instantaneous pressure fluctuation ($p' = p(t) - \bar{p}$)

At $x/c = 0.2$ on the suction side within the laminar boundary layer, Fast Fourier Transformation (FFT) of the pressure histories has been performed. In Fig. 4 the corresponding results are shown for all meshes. For displaying purpose, the meshes M2, M3 and M4 have an artificial offset of the nondimensionalized ampli-

tude p_A of 0.001, 0.002 and 0.003, respectively. The mesh M5 yield shorter simulation periods resulting in coarser resolution of the FFT, especially for low frequencies. Therefore, this FFT is not shown. In all FFTs the pressure waves effect peaks in the range of $1000\ Hz < f < 5000\ Hz$. The investigation of the original pressure signal shows steepened pressure waves at this frequency denoting that the peaks in the FFT is caused by pressure waves and not by disturbances within the boundary layer. The results for M1 identify a dominant frequency at $f = 1000\ Hz$, which is not detectable for finer meshes. This means that the generation mechanism of the pressure waves is influenced by the low mesh resolution. The FFTs for the meshes M3 and M4 show the highest peak around $f = 2500\ Hz$. Also, the amplitude equals for both meshes. Since the pressure waves are generated at the TE by an interaction of the turbulent and the transitional boundary layer, a wrong TS-wave frequency of the transitional boundary layer might be a possible explanation for this. However, the general appearance of pressure waves seems to be very insensitive to the mesh resolution.

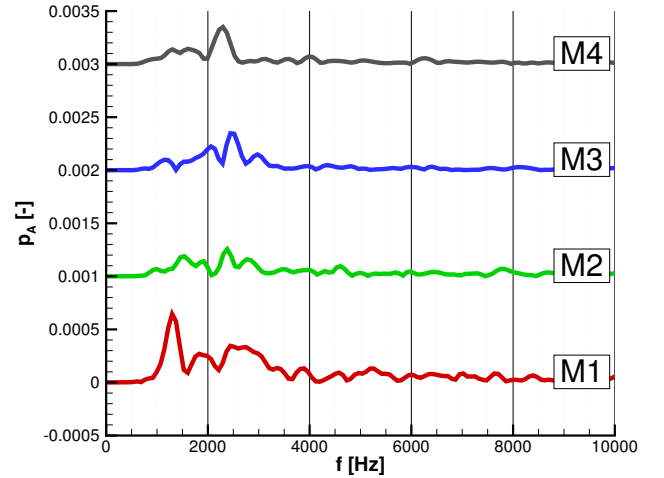In the following, the boundary layer flow and its turbulent quantities are studied.

Fig. 4: FFT of pressure history taken at $x/c = 0.3$, $\Delta y_{wall}/c = 0.002$, $z/c = 0$

First, the thickness of the boundary layer δ_{99}, the displacement δ^* and the momentum thickness Θ are studied along the suction side of the airfoil (Fig. 5). The region of the transition area is distinguishable in the δ^* graph. Furthermore, the graphs of Θ and δ_{99} show a bending at the location of transition $x/c \approx 0.5$. Comparing the results of all meshes with each other, the coarser meshes overestimate δ^* but underestimate and Θ. Beside M1, the results of δ_{99} agree very well.
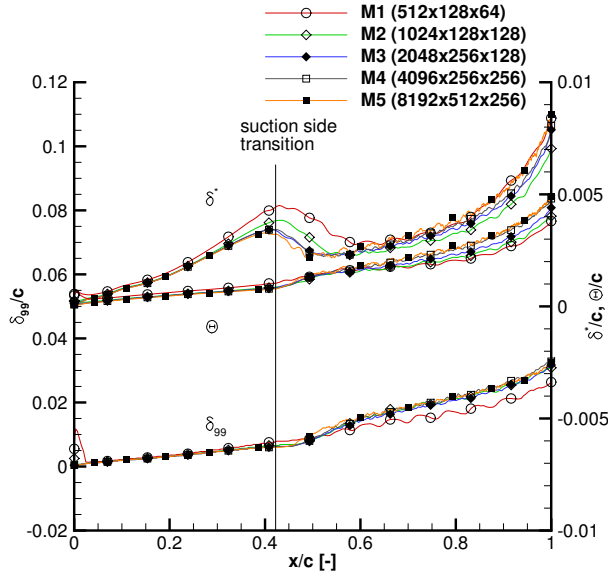
Fig. 5: Boundary layers thicknesses δ_{99}, δ^* and Θ along suction side

Fig. 6: Mean velocity profile at $x/c = 0.71$

In Fig. 7 the nondimensionalized averaged turbulent kinetic energy $\overline{k} = 0.5 \cdot \left(\overline{u'u'} + \overline{v'v'} + \overline{w'w'} \right)$ is plotted versus the distance from the wall Δ related to the boundary layer thickness δ_{99}. The results are temporal averaged over the last 100 data sets. Beside the temporal averaging of k, a further spatial averaging over the whole span is performed. For all meshes, k rises to a maximum k_{max} and vanishes outside of the boundary layer. The meshes M4 and M5 reach k_{max} at $\Delta/\delta_{99} = 0.05$, M2 and M3 slightly above at $\Delta/\delta_{99} = 0.06$ and M1 at $\Delta/\delta_{99} = 0.11$. The value of k_{max} is approximately 0.0135 for all meshes.

Since the boundary layer integral values do not show large differences between the results, in the following, the different parameters within the turbulent boundary layer are considered. In Fig. 6 the boundary layer u^+ profiles for the position on the suction side at $x/c = 0.71$ are plotted in wall units. Additionally, the corresponding results of Spalart's DNS [7] of a flat plate are illustrated. The results of Spalart and the one for the mesh study, show at this location a Reynolds number of approximately $Re_\delta^* = 2000$ and $Re_\delta^* = 1500$, respectively. The results for M1 is far away from all other graphs. The difference between the remaining meshes can be seen at higher values for y^+ because the growth rate in wall-normal direction differs. In the buffer layer $(5 < y^+ < 50)$ and the log-law region $(y^+ > 50)$ the differences become more obvious. The results of the meshes having the same number of spanwise mesh points agree well demonstrating again the importance of the spanwise resolution. The log-law behaviour, shown in Spalart's results, is not even reached for the finest meshes. Considering a transonic airfoil flow, the disagreement can be explained by the compressibility and by a non-zero pressure gradient. Sandberg's [8] mean velocity profiles from a DNS of the NACA 0012 airfoil demonstrate the same trends.
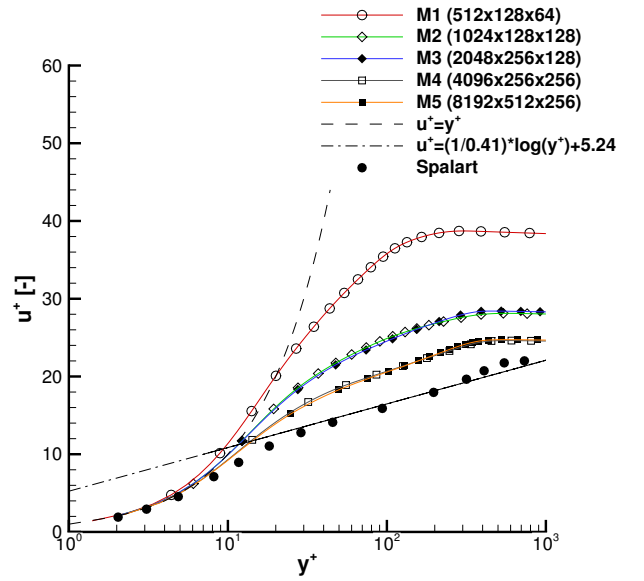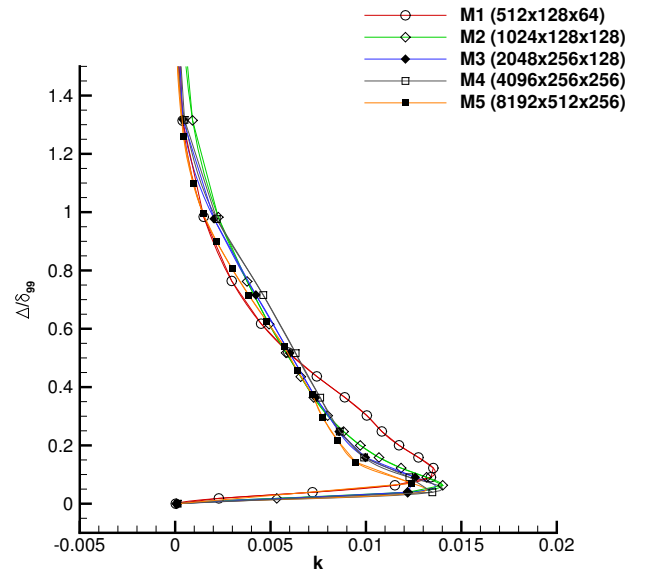

Fig. 7: Averaged profiles of turbulent kinetic energy at $x/c = 0.71$

The averaged Reynolds stresses normalized by the turbulent kinetic energy are plotted in wall units. The averaging is identical to the one before. For coarse meshes, the Reynolds stresses $\overline{u'u'}/k$ are overestimated. The Reynolds stresses $\overline{v'v'}/k$ and $\overline{w'w'}/k$ tend to be underestimated. This linkage between mesh resolution and the Reynolds stresses is also observed by Fröhlich [9].

Showing only slight differences, the graphs of M4 and M5 agree well over the whole boundary layer. The results for M2 and M3 demonstrate for the whole boundary layer differences to M4 and M5. The coarser the mesh, the larger is the difference to M4 and M5. Again, the coarsest mesh M1 shows the largest error related to M4 and M5. For the remaining meshes M2-M5 the graphs for $\overline{u'u'}/k$, $\overline{v'v'}/k$ and $\overline{w'w'}/k$ are in principle agreement with literature [10].
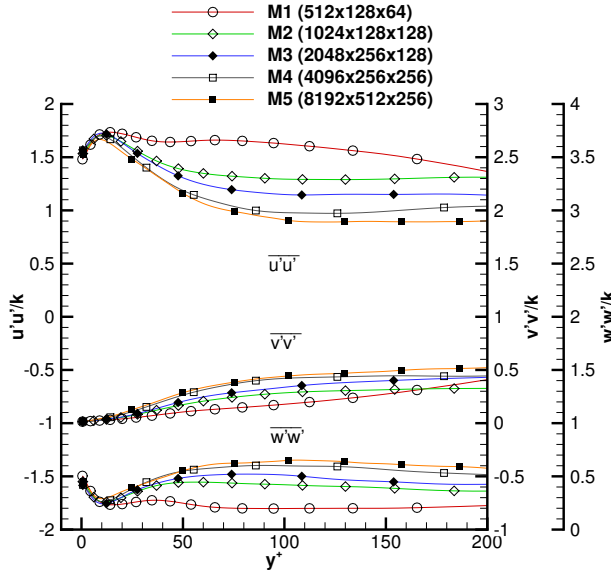

Fig. 8: Averaged profiles of Reynolds stresses normalized by k at $x/c = 0.71$

Next, three one-dimensional energy cascades (Figs. 9, 10, 11) of the turbulent kinetic energy are shown to study the turbulent behaviour of the flow in full detail. The spectra have been determined at the same wall distance $\Delta y_{wall}/c = 0.0065$ of the suction side for all considered meshes, which for mesh M5 is equivalent to $y^+ = 120$. Considering spectra within the outer boundary layer, the $-5/3$ behaviour is expected to extend over a wide frequency and wavenumber range. The spatial spectra are averaged over 10 data sets at intervals of $\Delta t = 0.2025c/u_\infty$. The spanwise spectra are taken over the whole span at $x/c = 0.71$ and the streamwise spectra in the range of $0.5 < x/c < 1.0$ at $z/c = 0$. The frequency spectra are taken at $x/c = 0.9$ and $z/c = 0.05$. In order to improve the quality of the spectra, a hanning window is applied. Furthermore, the signal of the turbulent kinetic energy is divided into two and four segments, which overlap with

50%, for spatial and frequency spectra, respectively. The spatial wavenumbers κ are related to the Kolmogorov microscale $\eta = L_{ref}/Re^{3/4} = 5.3 \cdot 10^{-5}c$. The energy is related to ηu_τ^2 with the nondimensional friction velocity $u_\tau = 0.043$ taken from results for mesh M5.

In theory, the energy cascade consists of three ranges. First, the small wavenumbers/frequencies form the energy-containing range. Next, larger wavenumbers/frequencies form the inertial subrange, that is indicated by the $-5/3$ slope in Figs. 9, 10, 11. In this range the eddies disintegrate from large into small eddies. At large wavenumbers/frequencies, in the dissipation range the eddies dissipate and the graphs peel off the slope of $-5/3$. In all figures, it is obvious that higher mesh resolutions extend the inertial subrange and move the dissipation range to higher wavenumbers. This is reasonable since finer meshes can resolve small eddies which dissipate on coarse meshes.

The orders of roll-off with increasing wavenumber and frequency are listed in Tab. 3. Having small $\Delta \tau$ as a result of the high Reynolds number, very high frequencies are resolved. In Jones DNS [11] of an airfoil flow the energy roll-off order for the spanwise and frequency spectra are 3 and 7, respectively. The presented results, shown in Tab. 3, show a comparable order of eddy decay.

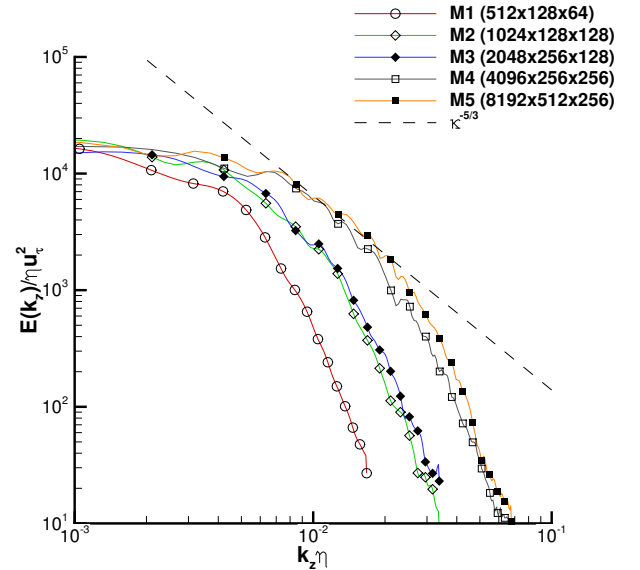| Mesh	κ_z	κ_x	f
Mesh 1 (M1)	3	2	7
Mesh 2 (M2)	3	2	7
Mesh 3 (M3)	3	3	7
Mesh 4 (M4)	3	3	7
Mesh 5 (M5)	3	4	7

Tab. 3: Orders of roll-off

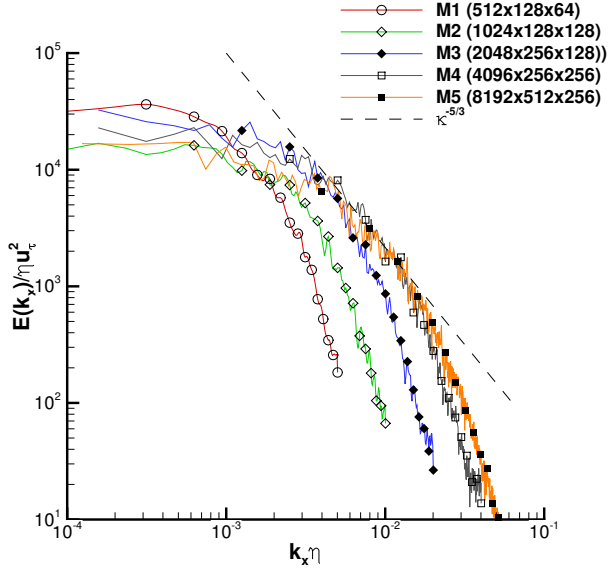Fig. 9: Spanwise power spectra of k, taken at $x/c = 0.71$, $y^+ = 120$

Fig. 10: Streamwise power spectra of k, taken in range of $0.5 < x/c < 1.0$ at $z/c = 0.0$, $y^+ = 120$

Fig. 11: Frequency power spectra of k, taken at $x/c = 0.9$, $z/c = 0.05$, $y^+ = 120$

Studying the spanwise spectra in Fig. 9, it is clearly ascertainable that the results for the meshes M4 and M5 are over a wide range approximately identical. The meshes M1-M3 yield identical results in the energy-containing range but show differences in the other ranges. For the finest meshes M4 and M5, the $\kappa^{-5/3}$ behaviour is easily detectable. Although the results for the meshes M4 and M5 agree well, this is no proof for a converged solution since its spanwise resolution is identical. Again, the results of the meshes having the same number of spanwise mesh points agree well and show the same maximal wavenumber.

In Fig. 10, the streamwise wavenumbers are analyzed. In contrast to Fig. 9, for the considered direction, all meshes have a different resolution, and no graphs are identical. Slightly diverging in the dissipation range, the graphs for M4 and M5 indicate that the solution is close to be mesh converged. The differences between M4 and M5 are quite small. The results of the meshes M4 and M5 follow the slope $\kappa^{-5/3}$ over a wide range.

Studying the frequency spectra in Fig. 11, it has to be noted that the simulations for all meshes are performed using the same nondimensional temporal step size $\Delta\tau = 4.5\cdot10^{-5}$. Therefore, the temporal resolution is identical for all meshes. The differences in the energy content is a result of the unequal spatial resolution. Depending on the total number of mesh points, the results show different ranges of the inertial subrange. The coarser the mesh, the lower the frequency at which the dissipation range begins. M4 and M5 demonstrate nearly the same frequency range for the beginning of the dissipation range.
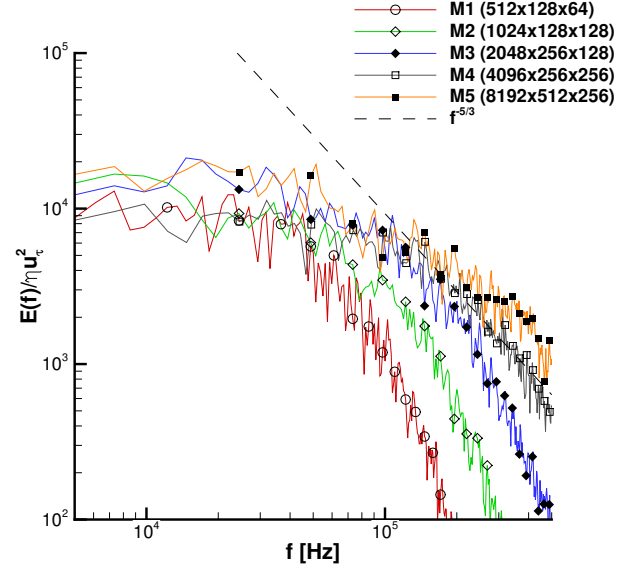
In the spatial and the frequency spectra, as expected the coarser meshes are not able to resolve the small eddies and show the start of the dissipation range for lower wavenumbers/frequencies. As a result, the viscosity of the flow is numerically increased and the kinetic energy of not resolved eddies dissipates into heat. This is even detectable in the visualization of the coherent structures of the boundary layers, shown in Fig. 3a,b. For the highly refined meshes, the turbulent boundary layer consists of distinguishable smaller structures.

In Figs. 9 and 10 the largest wavenumbers do not reach $\kappa\eta = 1$. Considering homogeneous and isotropic turbulence, in theory, at this wavenumber the dissipation range begins since the smallest eddies have a size of η. These large wavenumbers are not reached because the spanwise and streamwise resolution in wall units, shown in Tab. 2, are above unity. For the finest mesh M5, the spanwise and streamwise wall units are in the order of 10. Accordingly, in Figs. 9 and 10 the largest spanwise and streamwise wavenumbers reach approximately 0.1. Although the theoretical optimal mesh resolution is not reached, the meshes M4 and M5 peel off the $\kappa^{-5/3}$ slope at $\kappa\eta \approx 10^{-2}$. It is assumed that this is not caused by the mesh. Firstly, both meshes yield a sufficient number of larger wavenumbers that could resolve a further energy transfer to smaller eddies. Secondly, both meshes peel off at the same wavenumber indicating that the reason is not the streamwise mesh resolution which is different for both meshes.

4 Conclusion

For the transonic flow around the NACA 0012 airfoil at the transonic flow condition $M_\infty = 0.65$, $Re_c = 5\cdot10^5$

and an angle of incidence of $\alpha = 2°$, a mesh study for a Direct Numerical Simulation is performed. The spatial derivatives of first-order are approximated by a fifth-order WENO scheme, the second-order derivatives by a sixth-order central scheme and the time derivatives by a fourth-order Runge-Kutta scheme. Consisting of 4(M1), 17(M2), 67(M3), 268(M4), 1.074(M5) million mesh points, five meshes are studied. In the first part of the results, common aerodynamic parameters (c_p, c_f) are studied and only small differences are detectable for the different meshes. Also, the study of the boundary layer thickness δ_{99}, the displacement thickness δ^* and the momentum thickness Θ along the suction side shows only slight differences. Nevertheless, studying the turbulent boundary layer near the TE in more detail, a disagreement between the meshes becomes visible. The results for the coarsest mesh M1 illustrate that the turbulent behaviour is not resolved correctly. This could already be seen from the flow visualization of the turbulent structures by using the Q-criterion. For the meshes M3, M4 and M5 the agreement is better. The spectra of the averaged turbulent kinetic energy demonstrate for low wavenumbers and frequencies a good agreement for these meshes indicating that these turbulent structures are resolved correctly. Here, the meshes M1 and M2 are clearly apart. For higher frequencies, especially in the dissipation range, the graphs diverge. In all spectra the log-law behaviour $k^{-5/3}$ can be identified showing that the inertial subrange of the spectra is resolved correctly.

Furthermore, the profiles of the turbulent kinetic energy, the mean velocity and the Reynolds stresses are in good agreement for the meshes M4 and M5. Slight differences are visible but over wide parts of the boundary layer these parameters are in good agreement. Although the mesh study showed only partly convergence, it is reasonable to assume that further mesh refinements will not show significant differences to the presented meshes. The number of mesh points in streamwise and wall-normal direction yield a converged solution and only in spanwise direction a further refinement could be useful. The spectra for the kinetic energy could show further improvements for high wavenumbers/frequencies, but the aerodynamic parameters and boundary layer profiles are nearly converged.

Acknowledgments

LITERATURE

Literatur

[1] H. Choi and P. Moin, "Grid-point requirements for large eddy simulation: Chapman's estimates revisited," *Physics of Fluids*, Vol. 24, no. 1, p. 011702, 2012.

[2] P. Tucker and J. DeBonis, "Aerodynamics, computers and the environment," *Philosophical Transactions of the Royal Society A: Mathematical, Physical and Engineering Sciences*, Vol. 372, no. 2022, p. 20130331, 2014.

[3] S. Lele and J. Nichols, "A second golden age of aeroacoustics?," *Philosophical Transactions of the Royal Society A: Mathematical, Physical and Engineering Sciences*, Vol. 372, 2014. Online publication date: 14-Jul-2014.

[4] P. Moin and K. Mahesh, "Direct numerical simulation: a tool in turbulence research," *Annual Review of Fluid Mechanics*, Vol. 30, no. 1, pp. 539–578, 1998.

[5] V. Hermes, I. Klioutchnikov, and H. Olivier, "Numerical investigation of unsteady wave phenomena for transonic airfoil flow," *Aerospace Science and Technology*, Vol. 25, no. 1, pp. 224 – 233, 2013.

[6] G. Jiang and C. Shu, "Efficient implementation of weighted Eno schemes," *Journal of Computational Physics*, Vol. 126, no. 1, pp. 202–228, 1996.

[7] P. R. Spalart, "Direct simulation of a turbulent boundary layer up to $Re_\theta = 1410$.," *Journal of Fluid Mechanics*, Vol. 187, no. 1, pp. 61–98, 1988.

[8] R. Sandberg, L. Jones, and N. Sandham, "Direct numerical simulations of noise generated by turbulent flow over airfoils," in *14th CEAS/AIAA Aeroacoustics Conference*, 2008.

[9] J. Fröhlich and W. Rodi, "Introduction to large eddy simulation of turbulent flows," in *Closure Strategies for Turbulent and Transitional Flows* (B. E. Launder and N. D. Sandham, eds.), pp. 267–298, Cambridge University Press, 2002. Cambridge Books Online.

[10] S. B. Pope, *Turbulent flows*. Cambridge University Press, 2000.

[11] L. Jones, R. Sandberg, and N. Sandham, "Direct numerical simulations of forced and unforced separation bubbles on an airfoil at incidence," *Journal of Fluid Mechanics*, Vol. 602, p. 175, 2008.